

Ductile to brittle transition in ITER specification tungsten assessed by combined fracture toughness and bending tests analysis

Chao Yin^{a,b,*}, Dmitry Terentyev^a, Thomas Pardoën^b, Roumen Petrov^c, Zhenfeng Tong^d

^a Structural Materials Group, Institute of Nuclear Materials Science, SCK•CEN, 2400 Mol, Belgium

^b Institute of Mechanics, Materials and Civil Engineering, UCLouvain, 1348 Louvain-la-Neuve, Belgium

^c Department of Electrical Energy, Metals, Mechanical constructions & Systems, Ghent University, 9052 Ghent, Belgium

^d China Institute of Atomic Energy, 102413 Beijing, China

ARTICLE INFO

Keywords:

Tungsten
Bending test
Fracture toughness
Ductile to brittle transition temperature
Fracture behavior

ABSTRACT

The evaluation of the fracture toughness of tungsten is required for the design of plasma-facing components in order to ensure safe and durable operation in ITER reactor, being under construction in France. During operation, plasma facing materials will be exposed to cyclic thermo-mechanical loads combined with high energy neutron flux, which, in general, reduce the fracture toughness. Characterization of the degradation of the mechanical properties after exposure to the neutron flux involves time consuming and expensive procedures due to nuclear activation and special handling. Subsequently, development of sample miniaturization and protocols to reduce the volume of material under inspection is critical to speed up the progress in R&D. In this work, we propose a combined approach for the reconstruction of the fracture toughness – temperature curve, which is applied in the ductile to brittle transition temperature range. The approach consists of two steps: (i) application of the three point bending tests using miniaturized samples to reveal the transition temperature range on the basis of flexural strain data; (ii) execution of standardized fracture toughness tests at the upper temperature of the transition regime. The results allow the determination of the fracture toughness as a function of temperature with a reasonable accuracy. The validity of the approach has been demonstrated on two commercial tungsten grades produced according to ITER specification and tested in the as-fabricated state. The conclusions are supported by microstructural analysis performed on both standardized and miniaturized samples.

1. Introduction

The response of structural or functional materials to impact, cyclic deformation, thermal shock or mechanical loads is of practical concern for a variety of applications, including structural crashworthiness, ballistic events, explosive–structure interactions and, in general, in high temperature applications from jet turbines up to plasma technology. Often, high performance materials are heterogeneous or at least exhibit a complex microstructure if considered at the micro-scale, see the example of polycrystalline metals, fiber/particle reinforced composites, or metallic laminates (see e.g. [1–5]). The international program on fusion electric power is one of the examples where the application of materials in extreme environmental conditions cannot be avoided [6]. Tungsten (W) constitutes one of the materials that will play a key role in the implementation of ITER as well as in DEMO projects [7–9]. Tungsten is a promising plasma facing material for both divertor and first wall components because of its high melting temperature and resistance to

sputtering by low-energy ions. However, the relatively high ductile-to-brittle transition temperature (DBTT) of W, being around 300–400 °C [10], is an important concern for the designers, since the exploitation in the thermo-nuclear fusion environment will raise its DBTT even to a higher temperature as a result of neutron irradiation damage [11–13]. However, most of the irradiation and post-irradiation tests performed in the past do not cover the actual temperature range required for the ITER and DEMO programs. Furthermore, the tests were performed on materials with specifications no longer up to date given the lessons learned after recent high heat flux test and updates in the design of the Plasma Facing Components (PFC) utilizing W [14].

A modelling-based assessment of the structural integrity of the PFC, as an alternative to fully-representative experiments, can be performed based on fracture mechanics analysis using the finite element method, see e.g. [15]. Such dedicated study can assess the failure probability and lifetime of a component given the boundary conditions (i.e. loading scheme, temperature profile, damage rate, etc.). However, the intrinsic

* Corresponding author at: Structural Materials Group, Institute of Nuclear Materials Science, SCK•CEN, 2400 Mol, Belgium.

E-mail address: cyin@sckcen.be (C. Yin).

<https://doi.org/10.1016/j.msea.2019.02.028>

Received 9 December 2018; Received in revised form 7 February 2019; Accepted 8 February 2019

Available online 10 February 2019

0921-5093/ © 2019 The Authors. Published by Elsevier B.V. All rights reserved.

properties of materials constituting the PFC remain the critical input ensuring robustness of such models. That is why the determination of the basic properties of the materials being exposed to neutron irradiation is an unavoidable task in the assessment of the behavior of the full component. Given that neutron irradiation and post-irradiation examination (PIE) constitute costly and time-demanding experiments, the scientific community looks for alternative options such as usage of accelerated irradiation with ions (see e.g. [16–18]) or miniaturization of the specimens for neutron irradiation (see e.g. [19,20]). Whilst ion irradiation can probe very small volume (within micro-meter range), the implementation of the small specimen testing techniques (SSTT) based on neutron irradiation brings significant benefits in terms of cost and time required to assess material properties. Thus, SSTT is one of the focuses of the current research program on fusion material's development and qualification. One of the key elements in the SSTT is to align the testing protocols and procedures accounting for the currently available standards e.g. well-known ASTM standard. When it comes to the assessment of W for fusion applications, the most critical question is how to deduce DBTT and fracture toughness using SSTT and to align it with the standard Master Curve approach used earlier to characterize non-irradiated W (see [21–26]).

The Master Curve approach, which is included in the ASTM standard 1921 [27,28], is based on the weakest link theory and Weibull statistics. This method considers that the Weibull modulus is equal to 4 and the shape of the master curve is fixed. Moreover, the transition temperature (T_0) is defined as $100 \text{ MPa}\sqrt{m}$ for 25 mm thick specimen. However, this set of parameters for the master curve method is designed for steels within the ASTM standard. Although tungsten is a BCC metal, which shows a ductile behavior above certain temperature, it has a relatively low fracture toughness (lower than $100 \text{ MPa}\sqrt{m}$, see [21–26,29,30]) as compared to ferritic/martensitic steels at the same homologous temperature where the material exhibits ductile deformation. In addition, some brittle materials show different fracture strength distribution and the Weibull distribution is not always the most appropriate method [31–35]. Indeed, the application of the Weibull statistics requires sufficient number of data points to properly identify the Weibull modulus [36], which is a shape parameter determining the probability density function. Often, when it comes to the assessment of neutron irradiated materials, the number of specimens available is rather limited, hence sound assumptions about the Weibull modulus are needed. However, it is also known that the Weibull modulus depends on the test temperature [37], subsequently the use of a fixed modulus over a wide temperature range is hard to justify. Other distribution functions, like a normal distribution, can be applied instead of the Weibull distribution for brittle materials [31,33].

Beside the above discussed master curve approach, instead of utilizing the conventional fracture toughness testing procedure, the DBTT range can be determined by using three point bending tests (on the flat bar specimen without a notch). In a report by Lawrence Livermore national laboratory dealing with tungsten, the value of the flexural strain has been used as an indicator for the DBTT [38]. The DBTT was defined as the temperature at which the flexural strain is equal to or

higher than 5%, which had been applied later on by other researches for tungsten based materials [39,40].

In this work, we perform a combined analysis relying on the standardized fracture toughness tests and on three point bending (3PB) tests to deduce the DBTT of commercial pure tungsten. The key idea is to minimize the number of fracture toughness tests required to provide an assessment of DBTT thanks to the extra information gained through the 3PB tests. The fracture toughness tests and 3PB tests are referred to ASTM standard E1921, E1821 and E290, respectively [28,41,42]. All tests are accompanied by microstructural investigations confirming the fracture mechanism and therefore proving the appropriate determination of the transition temperature. By demonstrating reliable prediction of the DBTT with this approach, transfer can be made to application on neutron irradiated materials in order to reduce the total number of samples and tests. In order to ensure the technological impact of this work, we carry the study using two commercial tungsten grades produced according to the ITER specification [14] by European company Plansee and Chinese company AT&M.

2. Methodology and experimental details

2.1. Materials and microstructural analysis

The microstructure and fracture surface of the specimens are analyzed using a JEOL JSM6610 scanning electron microscope (SEM). The surface fraction of the different fracture patterns are quantified by ImageJ image analysis software. Electron backscattered diffraction (EBSD) is used to analyze the morphology and orientation of the grains. The measurements are performed based on the Bruker QUANTAX EBSD system, and OIM TSL analysis software is used to calculate Low angle grain boundary density (with a step size of $2.74 \mu\text{m}$) and to plot the inverse pole figure (IPF) after the EBSD measurements.

Two grades of commercially pure tungsten (W) processed according to the ITER specification [14] were studied. These grades will be referred to as IGP and CFETR, being manufactured by Plansee (Austria) and AT&M (China), respectively. Both materials were produced by powder metallurgy methods. The mechanical treatments are different: double hammering was applied to IGP W and rolling was applied to CFETR W. Their composition (provided by the manufacturer) and grain size are shown in Table 1; the grain characteristics are calculated by the MTEX Matlab code.

The microstructure of the two W materials can be analyzed based on the map of inverse pole figures (Fig. 1), where the color mapping is related to the orientation of grains. Because of the hot rolling (CFETR) and hot forging/hammering (IGP), the microstructure consists of essentially elongated grains whose axis coincides with the longitudinal direction. The grains are elongated, and therefore the measured medium diameter represents only the effective size, while the apparent size is essentially different. The main differences between these materials are (1) the grain shape aspect ratio in TD-LD plane (plane normal to ND), see Table 1; and (2) the texture, see Fig. 1c and d. The impact due to these differences will be discussed further after presentation and

Table 1

Composition and grain characteristics (normal to normal direction) of the W materials; the equivalent medium diameter is defined as the equivalent diameter of grains that have 50% cumulative area fraction; the median aspect ratio is defined as the ratio between the long side and the short side of an equivalent ellipse, which has the best match with the grain shape.

Materials	IGP						CFETR					
Composition	Pure W (> 99.97 wt%)						Pure W (> 99.94 wt%)					
Major impurities (maximum concentration, $\times 10^{-3}$ wt%)	C	O	N	Fe	Ni	Si	C	O	N	Fe	Ni	Si
	3	2	0.5	3	2	2	10	10	10	10	10	10
Plane normal to (the directions are shown in Fig. 2)	Normal direction			Transverse direction			Normal direction			Transverse direction		
Equivalent median diameter (μm)	101.88			95.02			77.88			62.12		
Median aspect ratio	9.79			10.75			2.42			7.43		
Low angle grain boundaries (LANGs) density (m^{-1})	2.17×10^5			2.01×10^5			2.20×10^5			2.03×10^5		

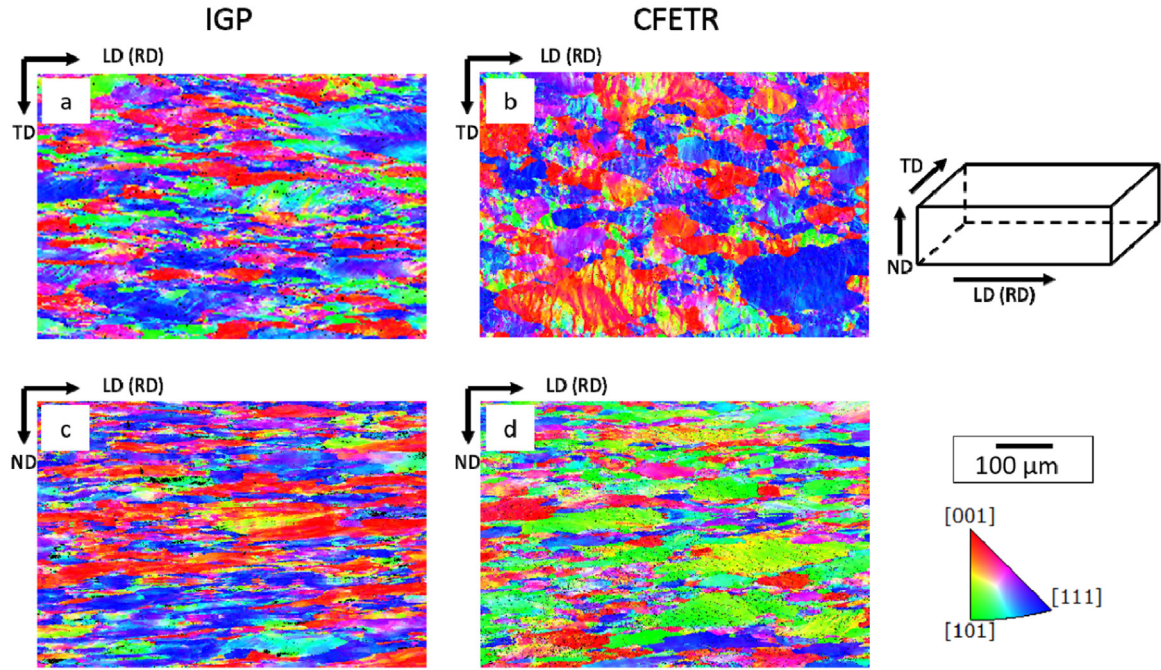


Fig. 1. Map of inverse pole figure of IGP and CFETR; (a) and (b) are normal to normal direction (ND); (c) and (d) are normal to transverse direction (TD).

analysis of the failure process. The microstructure of IGP material has been investigated by TEM revealing that the dislocation density is in the range of $(2 - 8) \times 10^{12} \text{ m}^{-2}$ [43]. Similar dislocation density is expected for the CFETR grade, but it is currently under investigation.

2.2. Specimens geometry and calculation method

Both disk-shaped compact tension (DCT) and 3PB specimens are machined with T-L orientation according to the ASTM E399 [44], as shown in Fig. 2. The DCT specimens were cut by electrical discharge machining (EDM) from the block materials (IGP was provided as rod with a 35 mm side square cross-section, CFETR as a 13 mm thick plate). The dimension ratio of the DCT specimens follows the ASTM standard. However, fatigue pre-cracking is not performed on the DCT specimens. Instead of fatigue pre-crack, an EDM cut notch with root radius around 50–90 μm is introduced into each DCT specimen. The sketch of the DCT specimen and the dimensions of the specimen are shown in Fig. 2 and Table 2.

The fracture toughness is calculated according to ASTM E1921 [28] and referring to ASTM E1820 [41]. The determination of fracture toughness in ASTM E1921 [28] is different from the one in ASTM E399

Table 2
Dimensions of DCT specimen.

	W	a_o	b_o	B
Dimension	~8.5 mm	~4.2 mm	~4.3 mm	~4 mm

[44] where the later considers a linear elastic behavior only. As a result, the fracture toughness value determined in ASTM E399 [44] is lower than the one determined in ASTM E1921 [28] when a specimen shows a non-linear load displacement response. The stress intensity factor rate during the elastic region is $0.43 \pm 0.08 \text{ MPa}\sqrt{\text{m}}/\text{s}$. The qualification of the fracture toughness K_{Jc} is based on the ASTM E1820 J_c criterion [41]: K_{Jc} can be defined if $b_o \geq 100J_{Qc}/\sigma_Y$, where J_{Qc} is the J-integral value without qualification and $\sigma_Y = (\sigma_{TS} + \sigma_{YS})/2$, where σ_{TS} is the ultimate tensile strength and σ_{YS} is the 0.2% offset yield strength. The fracture toughness K_{Jc} that does not meet the J_c criterion will be replaced by the highest K_{Jc} value at the same temperature that meets the criterion. This procedure is adopted from the ASTM E1921 [28] in order to determine the K_{Jc} -temperature curve within the transition temperature range rather than to find the upper shelf fracture toughness. Eq. (1) is used for

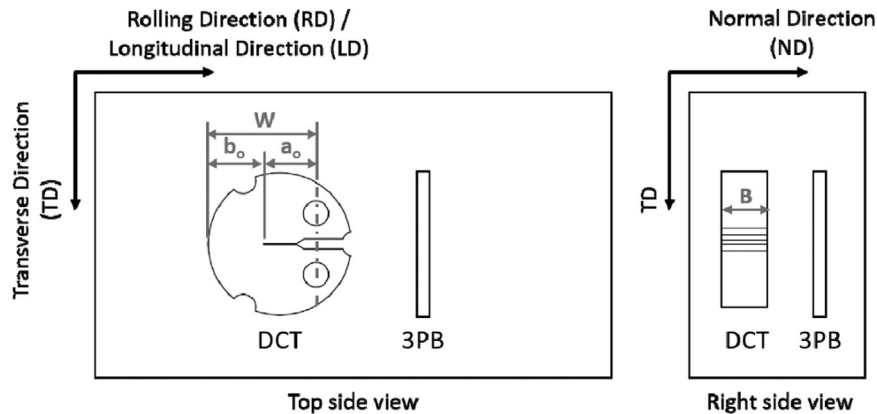


Fig. 2. Cutting scheme showing how test samples were fabricated given the longitudinal direction of the W products. The samples were cut by electric discharge machining.

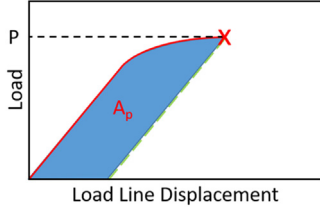


Fig. 3. Schematics of the mechanical load vs. load line displacement curve; P is the load when cleavage or any unstable cracking occur.

the determination of the fracture toughness K_{Jc} :

$$K_{Jc} = \sqrt{J_e \frac{E}{1-\nu^2}}, \quad (1)$$

where $J_e = J_e + J_p$, with J_e the elastic part of the J-integral, which can be deduced from Eq. (2) and J_p the plastic part of J-integral and can be calculated using Eq. (3). J_e is expressed as

$$J_e = \frac{(1-\nu^2)K_e^2}{E}, \quad (2)$$

in which ν is the Poisson ratio, E is the elastic modulus, and K_e is the linear elastic fracture toughness defined as the linear elastic equivalent stress intensity factor when the force equal to the fracture load P , as shown in Fig. 3. In the other hand, J_p is expressed as

$$J_p = \frac{\eta A_p}{Bb_0}, \quad (3)$$

where A_p is the work of plastic deformation, as shown in Fig. 3, $B \times b_0$ is the cross section of the ligament, and the parameter η is equal to $2+0.522\frac{b_0}{W}$.

The three-point bending test set-up is designed following the ASTM E290 standard [42]. The strain rate of the maximum tension part of the specimen is approximately 10^{-3} s^{-1} . The dimension of the 3PB specimen is $1 \text{ mm} \times 1 \text{ mm} \times 12 \text{ mm}$, which looks similar to a matchstick. The flexural strain (FS%) is calculated using Eq. (4) as

$$FS\% = \frac{6Dd}{L^2} \quad (4)$$

in which D is the maximum deflection of the 3PB specimen, d is the thickness of the specimen, and L is the supporting span of the test stage (in this case $L = 8.5 \text{ mm}$).

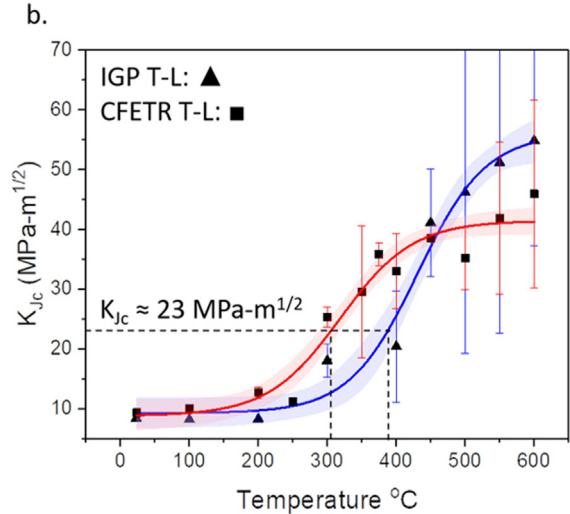
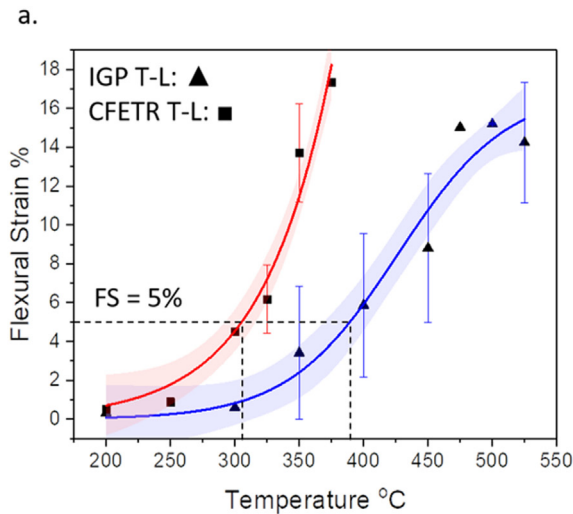


Fig. 4. (a) Variation of FS as a function of Temperature and (b) variation of K_{Jc} as a function of Temperature curve for IGP T-L (triangles) and CFETR T-L (squares) grades. The error bars in both figure represent one standard deviation of the experimental data. The pink and blue bands show the 68% confidence bands. (For interpretation of the references to color in this figure legend, the reader is referred to the web version of this article.)

The tests were performed in air in the temperature range RT to 600°C on a standard INSTRON 3800 universal mechanical testing machine.

2.3. Fitting method

In order to fit the dependence of K_{Jc} and flexural strain (FS) on test temperature, we use the mean values of the experimental results instead of the median values of the Weibull distribution. This choice is motivated by the limited number of tests performed at each temperature (1–6 samples were tested at each temperature). Later on, it will be shown that the two W materials exhibit different transition temperatures, and in the case of IGP that the flexural strain shows a plateau as the temperature reaches 525°C . On the other hand, the saturation of the flexural strain for CFETR is not attained yet at the highest flexural strain capacity of the test stage, which is around 20%. Because of this, two functions are exploited to fit the FS experimental results: (i) an exponential function (Eq. (5)) for CFETR and (ii) a Boltzmann sigmoidal function (Eq. (6)) for IGP. The experimental results of fracture toughness for both materials is fitted using a Boltzmann sigmoidal function (Eq. (7))

$$FS\% = FS_{base} + B \cdot \exp(C \cdot T) \quad (5)$$

$$FS\% = FS_{base} + \frac{FS_{top} - FS_{base}}{1 + \exp(C(T_{half} - T))} \quad (6)$$

$$K_{Jc} = K_{base} + \frac{K_{top} - K_{base}}{1 + \exp(C(T_{half} - T))} \quad (7)$$

where FS_{base} and K_{base} are constants that define the lowest values of FS and fracture toughness, FS_{top} and K_{top} are constants that define the highest values i.e. the values obtained at 600°C , B and C are deduced from the fitting procedure, the constant C will be referred to as the slope parameter, and T_{half} is the temperature of the inflection point (the temperature that the second derivative of the curve is equal to zero).

3. Results

3.1. Three-points bending tests

Fig. 4a presents the results of the three-point bending tests. The flexural strain increases exponentially with increasing temperature for both materials. As proposed by Lassila et al. [38], DBTT is in the range

Table 3
Parameters obtained from the best fit of the FS-Temperature curves.

Materials	Parameters					R ²
	FS _{base}	FS _{top}	B	C	T _{half}	
IGP T-L	0 ± 1.613	16.951 ± 3.649	–	0.023 ± 0.012	426.383 ± 25.208	0.958
CFETR T-L	0 ± 1.923	–	0.017 ± 0.038	0.019 ± 0.006	–	0.967

where the flexural bending strain reaches 5%. This temperature will be referred to as T_{5%}. This definition is different from the method used to find the DBTT through the fracture toughness tests, where the DBTT is considered to be the temperature at which linear elastic fracture mechanics (LEFM) is no longer valid [45,46] or the temperature corresponding to the maximum value of fracture toughness [47–49].

According to the results of 3PB tests, the transition is around 300 °C for the CFETR and around 400 °C for the IGP material. In the IGP grade, the Boltzmann sigmoidal function fits well the experimental results, while in the case of CFETR material the exponential function closely captures the experimental trend. The best fit parameters are collected in Table 3. Both fits have a R² value higher than 0.95, which indicates the good quality of the fit. According to the fitted curves, T_{5%} of IGP T-L is 389 ± 16/–19 °C and, T_{5%} of CFETR T-L is 305 ± 12 °C, which makes a difference of 85 °C.

3.2. Fracture toughness tests

The fracture toughness measured for both materials and presented in Fig. 4b is found to increase according to the Boltzmann sigma type function with temperature for IGP and for CFETR material. The parameters obtained by applying the fitting procedure are presented in Table 4. Just as in the case of flexural strain, the confidence factor R² exceeds 95%, hence we consider the fitting procedure to be reliable.

The rate at which the fracture toughness increases with temperature levels off at 400 °C for CFETR and at around 500 °C for the IGP material. Earlier studies on similar textured commercially pure W grades found the maximum of the fracture toughness in the temperature range of 600–800 °C [26,48]. The standard deviation on the mean value also increases with the test temperature. Statistical aspects become very important on the determination of K_{Jc} at high temperature.

Using the coefficients reported in Table 4, the fracture toughness of IGP and CFETR at T_{5%} is found to be 23.3 ± 3.8 MPa√m and 23.0 ± 2.3 MPa√m, respectively, hence, equal to one another. K_{top} is determined at the highest test temperature. The value of K_{base} should be close to the value predicted by the Griffith criterion considering a fully brittle material at 0 K. The surface energy G required to form the new open surfaces at fracture is around 3 J/m² [50]. Therefore, the fracture toughness K_e should be equal to 1.2 MPa√m for the “ideal” fully brittle tungsten. However, the experimental results, obtained at low temperature, do not match with the result coming from the Griffith limit because some degree of micro-plastic deformation still occurs at the crack tip of tungsten [24]. Hammering and/or rolling during the manufacture process indeed increases the fracture toughness of tungsten [24,25,47,51–54]. As a result, the obtained K_{base} is found to be 9 ± 2.7 MPa√m for technical grade tungsten and also is in line with other experimental data obtained earlier [21,22,26,48,55].

Table 4
The parameters of the fitted K_{Jc}-Temperature curve.

Materials	Parameters					R ²
	K _{base}	K _{top}	B	C	T _{half}	
IGP T-L	9.292 ± 2.352	55.994 ± 5.034	–	0.020 ± 0.008	431.040 ± 17.991	0.974
CFETR T-L	8.822 ± 2.613	41.442 ± 2.293	–	0.019 ± 0.006	318.966 ± 18.789	0.950

3.3. Fracture surface

To substantiate the results of mechanical testing and the approach of Lassila [38] regarding the determination of the transition temperature, we performed a detailed investigation of the fracture surface. Scanning electron microscopy analysis was performed on the materials deformed at low temperature (in the 100% cleavage region), near the transition temperature and at the upper studied temperature. Fig. 5 shows the fracture surface of both materials as obtained using the 3PB samples, which were tested near the T_{5%} temperature. Both intergranular and transgranular brittle fracture are observed on the fracture surface. However, the transgranular brittle fracture pattern of CFETR T-L is higher than the one of IGP T-L i.e. approximately 30% and 50% of the pattern correspond to the transgranular brittle fracture for IGP T-L and CFETR T-L, respectively.

The evolution of the DCT fracture surfaces of the IGP grade tested at 23, 400 and 600 °C are shown in Fig. 6. As the test temperature increases to 400 °C (i.e. close to T_{5%} of this material), the fraction of transgranular brittle fracture pattern increases from 10% to 20%, see Fig. 7. At 600 °C, delamination and dimples are clearly observed, which implies a ductile deformation behavior. However, the stability of the crack propagation process cannot be determined by characterization of the fracture surface. Further investigation of crack propagation, e.g. by means of video registration, is required.

The fracture surfaces of the CFETR grade tested at 23, 300 and 600 °C are shown in Fig. 7. The comparison between Figs. 7 and 6, shown that the evolution of the fracture surface pattern is different in the case of CFETR. At 300 °C (close to T_{5%}) both trans- and intergranular brittle fracture is observed (transgranular brittle fracture is around 30%). The pattern at 300 °C is different from the one at 23 °C, which shows high fraction of transgranular brittle fracture (60%). Whereas at 600 °C, no delamination is observed but just a mixture of transgranular brittle fracture (30%) and dimples is presented.

3.4. Texture

A deeper analysis of the crystallographic texture is performed as a starting point to explain the differences in the DBTT of IGP and CFETR grades. The inverse pole figure (IPF) indicates the intensity associated to crystallographic directions, which align toward the specific specimen orientation. The corresponding distribution of crystallographic planes normal to different crystallographic directions indicated on the IPF can also be identified.

As shown in Fig. 8, both materials exhibit a preferential texture on the fracture plane normal to TD. IGP appears to have high intensity of {001} and {111} crystallographic planes and high intensity of {101} crystallographic direction, as shown in Fig. 8a and b. Moreover, the IPF

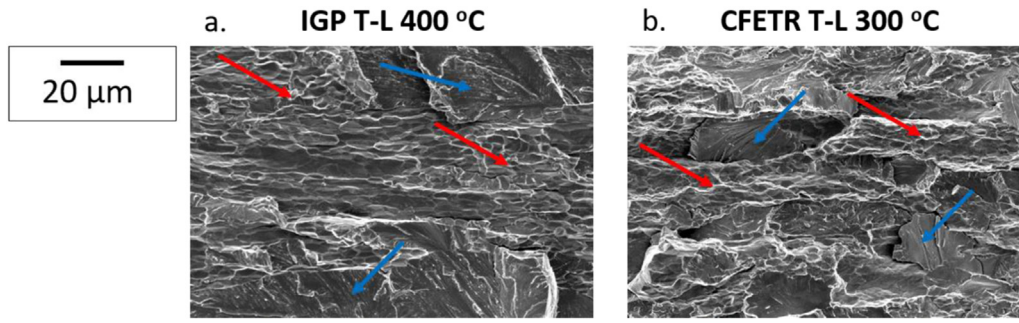


Fig. 5. The fracture surface of 3PB specimens obtained for (a) IGP at 400 °C and (b) CFETR at 300 °C, which is near $T_{5\%}$ as determined from mechanical tests. The red arrow indicates intergranular fracture failure; the blue arrow indicates transgranular brittle fracture. (For interpretation of the references to color in this figure legend, the reader is referred to the web version of this article.)

of IGP exhibits medium intensity of $\langle 001 \rangle$ crystallographic direction. Differently from the IGP, the CFETR material exhibits medium intensity of $\{001\}$ and $\{101\}$ crystallographic planes and high intensity of $\langle 101 \rangle$ crystallographic direction, as shown in Fig. 8c and d. The quantized intensity of crystallographic planes and crystallographic directions, which are analyzed by the crystal direction function of OIM TSL analysis software, are shown in Table 5. This information will be used later in the discussion of the results.

4. Discussion

4.1. Methodology to construct $K_{Jc}(T)$ curve by single temperature measurement

The purpose of this section is to summarize the results and to discuss how small specimen test configurations can be used to explore the transition temperature range in order to guide the standardized fracture toughness testing.

At first, the relationship between the fracture toughness K_{Jc} and flexural strain of the two tested materials is shown in Fig. 9a. One can see that the fracture toughness K_{Jc} of both materials is almost identical in the range of the low flexural strain (up to $\sim 5\%$). This can be explained by the grain properties. As shown in Table 1, the two tested materials have similar aspect ratio and similar density of low angle grain boundaries (LAGBs) over the fracture plane (ND-LD plane). As indicated in the literature, the aspect ratio [55] and dislocation sources e.g. LAGBs [47,49,51] do have an impact on the fracture toughness below the DBTT. Similarity of the microstructure of the two grades is likely the reason why the fracture toughness vs. FS of both materials at

low temperature (i.e. below $T_{5\%}$) is almost the same. At higher values of FS, the fracture toughness curve begin to deviate, which implies that the two materials show different sensitivity to strain state in the upper shelf regime.

Secondly, the slope parameter C (see Eqs. 5–7, Tables 3 and 4) was obtained from both 3PB and DCT tests. An easy way to compare the slope parameters obtained from the two types of tests is to plot the natural logarithm vs. test temperature as presented in Fig. 9b. The values of $\ln(K_B)$, $\ln(FS\%_E)$ and $\ln(FS\%_B)$ are derived from the equations used to fit K_{Jc} curves, and these values read:

$$\ln(K_B) = \ln\left(\frac{K_{Jc} - K_{base}}{K_{top} - K_{Jc}}\right) + CT_{half} = CT \quad (8)$$

$$\ln(FS\%_E) = \ln\left(\frac{FS\%}{B}\right) = CT \quad (9)$$

$$\ln(FS\%_B) = \ln\left(\frac{FS\% - FS_{base}}{FS_{top} - FS\%}\right) + CT_{half} = CT \quad (10)$$

where the constants B, C, K_{base} , and K_{top} are taken from Tables 3 and 4.

$\ln(K_B)$, $\ln(FS\%_E)$ and $\ln(FS\%_B)$ are plotted in Fig. 9b, and the figure clearly demonstrates the parameter C for CFETR T-L agrees much better than that for the IGP T-L. The deviation of the slope parameter from the two types of tests for IGP T-L can be explained by a relatively large dispersion of the fracture toughness values measured at high test temperature, as shown in Fig. 4b. In order to quantify the accuracy of the agreement of slope parameters of IGP T-L and to account for the relative error (calculated as propagated error of the slopes from the both tests), we propose to compare the convergence criterion

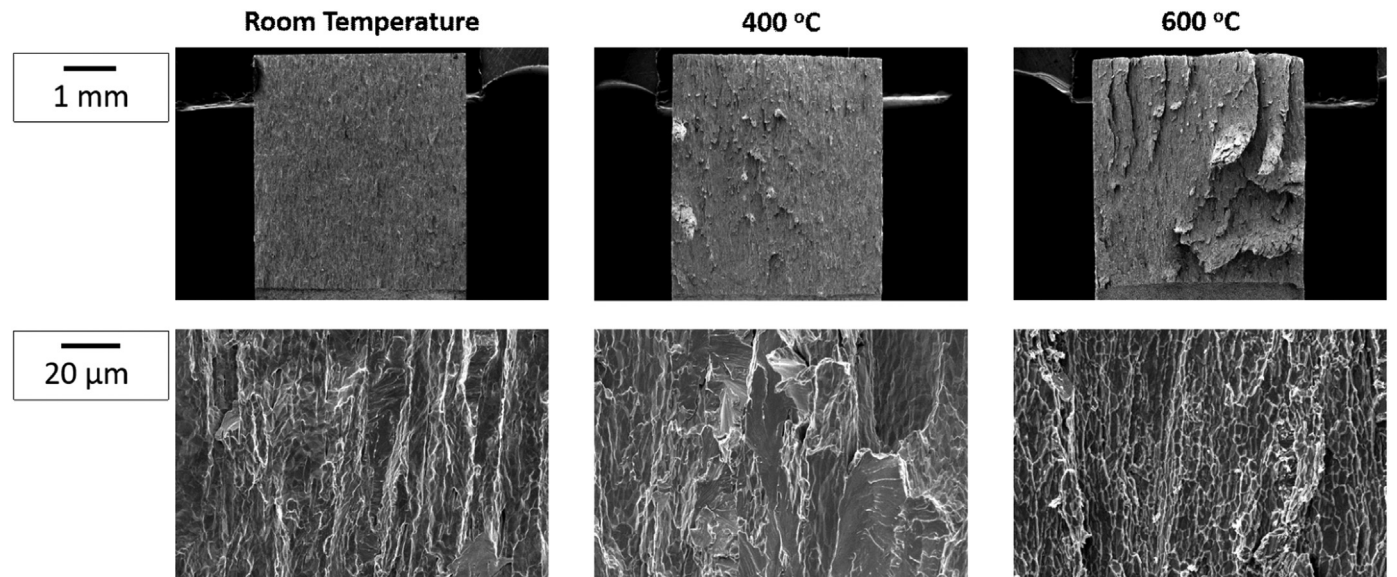


Fig. 6. Fracture surface of the DCT specimens of IGP material obtained at 22, 400 and 600 °C.

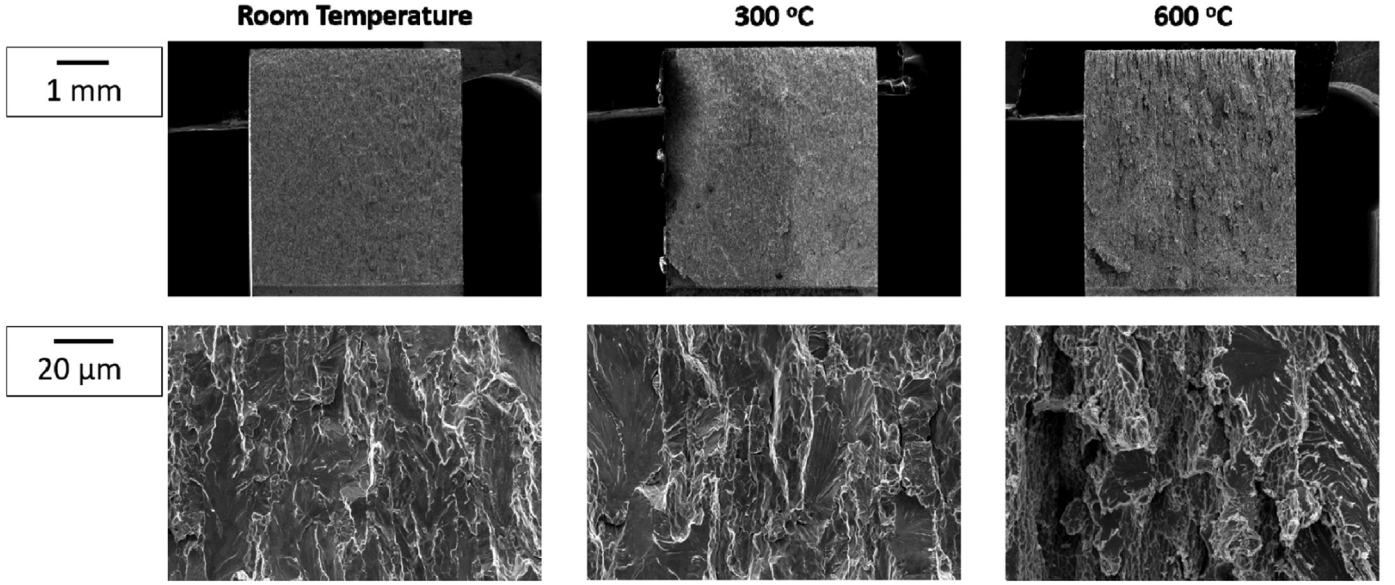


Fig. 7. Fracture surface of DCT specimens of CFETR material tested at 22, 300 and 600 °C.

$f = |1 - C_{FT}/C_{FS}|$ with this error (C_{FT} is the slope parameter of fracture toughness test, and C_{FS} is the slope parameter of three-points bending test). Following the rule of error propagation, the resulting error equals to $C_{FT}\sqrt{(\sigma_{FT}/C_{FT})^2 + (\sigma_{FS}/C_{FS})^2}/C_{FS}$ where σ_{FT} and σ_{FS} are the uncertainty of C_{FT} and C_{FS} , respectively, as shown in Tables 3 and 4. If the propagated error is larger than the convergence criterion f , the two slope parameters can be considered as agreed. The propagated error and f of IGP T-L are found to be 0.57 and 0.13, respectively. Hence, the slope parameters for the flexural strain obtained from the miniaturized 3PB tests are very close to the slope parameters measured for the fracture toughness using standardized DCT geometry. Because of this, the flexural strain measurements can be proposed as a complimentary method to define the transition temperature range and therefore to guide and minimize the number of fracture toughness tests to determine DBTT.

The complementary approach can be implemented in the following way. Since the slope parameters of both 3PB and DCT fracture toughness test are similar, and given that K_{base} is known, it should be possible to deduce the K_{Jc} -Temperature curve by performing a set of fracture toughness tests at a single temperature. Of course, this curve can be determined only in the transition temperature range and will not cover the temperature range where ductile tearing is observed. a

We now assess our approach on the example of the CFETR material, whose fracture toughness is best fitted by the Boltzmann sigmoidal function (Eq. (7)). The function requires four parameters: the slope parameter C , K_{base} , K_{top} , and T_{half} . The slope parameter C is taken from the 3PB tests (Table 3). As shown in Table 4, K_{base} for both materials is around $9 \text{ MPa}\sqrt{\text{m}}$. In order to assess the influence of this parameter on

the prediction of the K_{Jc} -Temperature curve, it is varied in the range of $5\text{--}10 \text{ MPa}\sqrt{\text{m}}$. K_{top} and T_{half} are calculated from the following equations:

$$K_{top} = \frac{K_{Jc1} - \alpha K_{Jc2}}{1 - \alpha} \quad (11)$$

$$T_{half} = T_2 + \frac{\ln\left(\frac{K_{top} - K_{Jc2}}{K_{Jc2} - K_{base}}\right)}{C} \quad (12)$$

where K_{Jc1} is the fracture toughness at temperature equal to $T_{5\%}$, which is equal to $23 \text{ MPa}\sqrt{\text{m}}$, the constant α is equal to $\exp\left[CT_2 - CT_1 + \ln\left(\frac{K_{Jc1} - K_{base}}{K_{Jc2} - K_{base}}\right)\right]$, and K_{Jc2} has to be obtained by the fracture toughness tests at T_2 . The temperature T_2 can be selected according to the transition temperature range determined from 3PB tests.

For instance, if T_2 is taken equal to 550°C , the constructed functions for both CFETR and IGP materials are shown in Fig. 10. The predicted curves of both materials match reasonably well the experimental points in the transition temperature range. The variation of K_{base} does not have a strong influence on the K_{Jc} curve in the transition temperature range. As a result, the shift of the DBTT after irradiation can be determined using the same methodology in two steps. In step 1, a set of 3PB tests is performed to identify the transition temperature range, slope parameter C , $T_{5\%}$ and T_2 . In step 2, a set of fracture toughness tests is performed at T_2 to deduce K_{top} and T_{half} . The selection of T_2 is very important since it must be higher than the DBTT but still comply with the criteria of validity of K_{Jc} according to ASTM E1820. Moreover, the fracture toughness has a larger spread at high temperature. Therefore, a sufficient

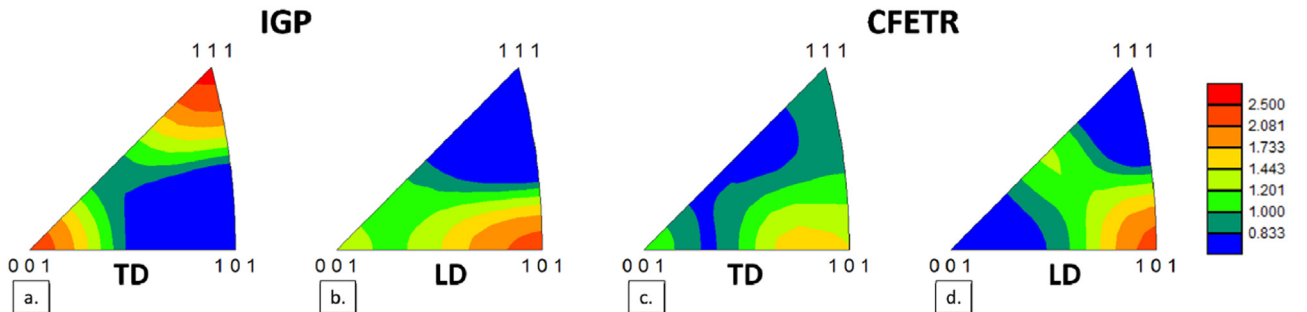


Fig. 8. Inverse pole figure for (a, b) IGP and (c, d) CFETR materials.

Table 5

Fraction of crystallographic planes normal to TD and fraction of crystallographic directions parallel to LD (with the $\pm 15^\circ$ of angular range from the reference crystallographic planes or reference crystallographic directions).

	Fraction of planes normal to TD			Fraction of directions parallel to LD		
	{001}	{101}	{111}	$\langle 100 \rangle$	$\langle 101 \rangle$	$\langle 111 \rangle$
IGP	0.174	0.046	0.269	0.118	0.326	0.019
CFETR	0.090	0.276	0.118	0.065	0.316	0.047

number of specimens (at least 3 specimens) is required to reliably determine a K_{Jc2} value.

The main objective of this approach is to reduce the number of test specimens required to assess the DBTT shift after neutron irradiation. With this respect, three important warnings regarding the proposed approach should be mentioned:

- the application of the equivalent slope C for non-irradiated and irradiated materials implies that the ductile-to-brittle transition is controlled by the same type of thermally activated mechanisms (e.g. activation of screw dislocation movement). Should the irradiation change the main mechanism of the plastic deformation, the C parameter must be redefined, which can be done by 3PB tests. In this case, the assessment of the microstructure becomes important and extra information to substantiate the mechanical testing procedure is required.
- the assumption that K_{base} for irradiated materials is the same as that for non-irradiated material remains valid as long as the grain microstructure and texture is not altered by the irradiation. In the case of irradiation at high temperature, removal of texture and some partial recrystallization may happen in addition to the formation of neutron irradiation defects. In this situation, the ambient microstructure (i.e. grain size, grain shape, dislocation density) before and after irradiation will no longer be the same and hence K_{base} can differ as well. However, a moderate variation of K_{base} (i.e. 5–10 $\text{MPa}\sqrt{\text{m}}$) does not lead to the strong impact of the transition temperature, as shown above.
- besides the shift of DBTT after neutron irradiation, the upper shelf of the fracture toughness is also known to decrease. Therefore, the approach requires further validation whether the K_{Jc} value at $T_{5\%}$ for neutron irradiated material is equal to 23 $\text{MPa}\sqrt{\text{m}}$.

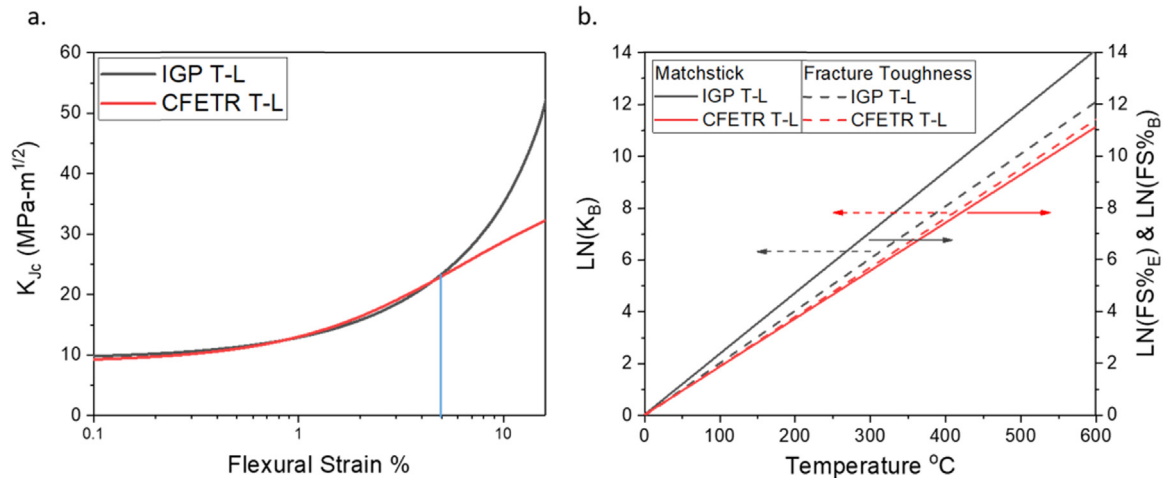


Fig. 9. (a) Variation of K_{Jc} as a function of flexural strain; (b) variation of natural logarithm of Exponential and Boltzmann sigma parameters as a function of temperature for both tested materials.

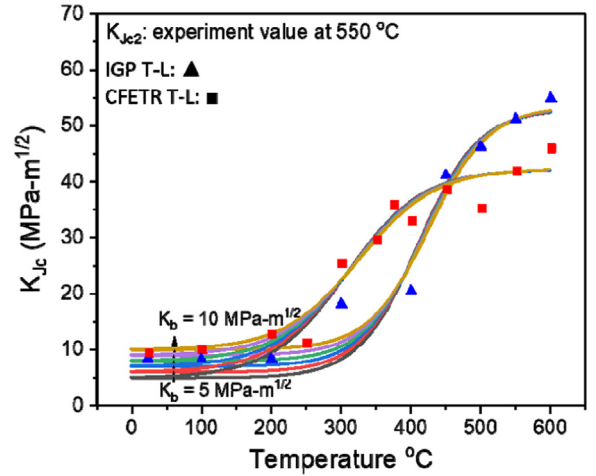


Fig. 10. Boltzmann sigma curve single temperature fitting approach.

4.2. Linking microstructure and fracture mechanism

The results of the mechanical tests show a difference of 85 $^\circ\text{C}$ in the DBTT (determined by $T_{5\%}$) and in the fracture behavior between IGP and CFETR grades. As summarized by Bonnekoh, et al. [56,57], the DBTT can be influenced by aspect ratio of the grains, impurities, lattice defects, and crystallographic texture (the degrees of impact decreases respectively). Since the density of LAGBs, initial density of dislocations and grain size aspect ratio of both materials on fracture plane (ND-LD plane) are similar, the difference in the DBTT could originate from impurities and crystallographic texture.

Because of the difference in the manufacturing process, the microstructure of the IGP and CFETR materials differs as well, as shown in Fig. 1. The grains of IGP exhibit a carrot-like shape, while the CFETR T-L grains have pancake-like shape. Following the literature [30,45–47,51,52,58], the fracture toughness and the DBTT depend on the crystallographic plane and direction along which the crack(s) propagate. For example, the activation energy for the ductile to brittle transition (Q_{DBT}) in the case of {001} $\langle 100 \rangle$ crack system (where {001} is the fracture plane and $\langle 100 \rangle$ is the crack propagation direction) is higher than for the {110} $\langle 1\bar{1}0 \rangle$ crack system [46,47,51]. Moreover, from the results of Gumbsch, et al. [47], the crystallographic direction, in which the crack propagates, has stronger influence on the DBTT than the crystallographic plane that is parallel to the crack surface. The effect of texture on DBTT can be observed from IGP materials, which has high

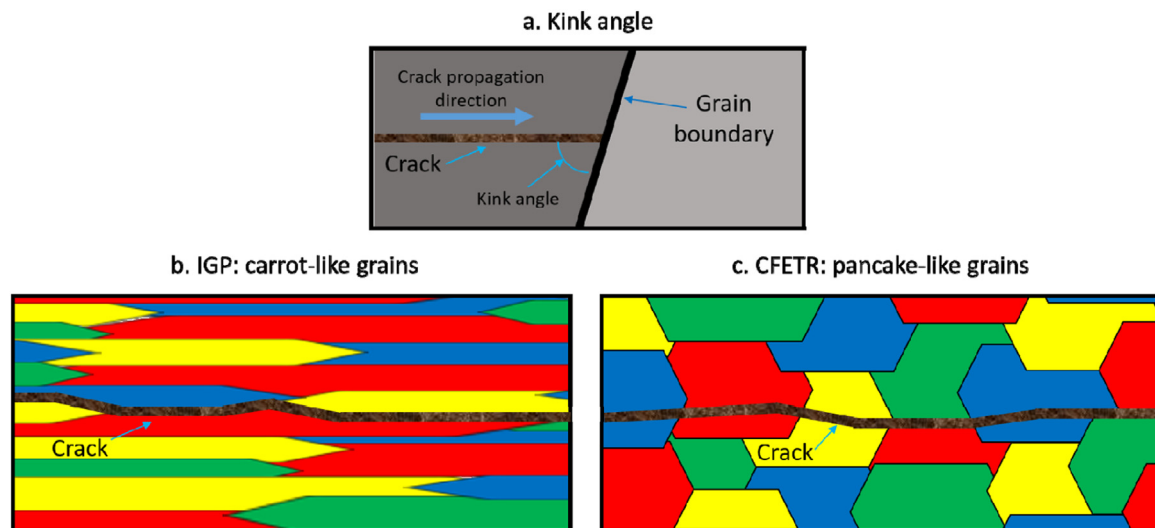


Fig. 11. (a) Kink angle between grain boundary and crack propagation direction; (b) IGP and (c) CFETR are the scheme of crack propagation route in TD-LD plane at low temperature.

fraction of $\{001\}$ planes (higher DBTT than $\{110\}$ planes if the crack propagation direction is $\langle 100 \rangle$ [47]) along the fracture plane and a high fraction of $\langle 100 \rangle$ directions (higher DBTT than $\langle 110 \rangle$ directions [47]) along LD (crack propagation direction), as indicated from Table 5. And these high fraction of $\{001\}$ planes and of $\langle 100 \rangle$ directions can be the reason why the IGP has higher DBTT than CFETR. Thus, the difference in the texture of IGP and CFETR provides an explanation of the reasons for the difference in the DBTT and in the fracture surface pattern.

Besides crystallographic texture, one should keep in mind that the two materials have slightly different chemical composition. However, at temperature significantly below the DBTT (for instance, room temperature), the effect of impurities on the fracture behavior can be ignored [59]. Therefore, the main factor that influences the fracture behavior is likely the orientation and morphology of grains, which is known to play a key role [21,23,55,60]. As indicated by Prakash et al. [60], the intergranular failure will occur in the fracture process zone if the kink angle between grain boundary and crack propagation direction (see Fig. 11a) is smaller than a threshold angle (the threshold angle is around 50° and will be smaller if the cohesive strength of grain boundary is higher); in other words, the grain will have transgranular brittle failure if the kink angle is larger than the threshold angle.

In the ND-LD plane, the fracture surface of IGP T-L exhibits a very high fraction of intergranular fracture (around 90%) because the material has carrot-like grains (high aspect ratio, as shown in Table 1) along the crack propagation direction; as a result, the kink angle is very small, as shown schematically in Fig. 11b. Unlike IGP T-L, CFETR T-L samples have pancake shaped grains (low aspect ratio, as shown in Table 1), which are oriented normal to the fracture surface. Consequently, the kink angle is higher in most of the cases, as shown in Fig. 11c. And in agreement with this, the fracture surface of CFETR T-L shows higher fraction of transgranular brittle fracture (around 60%) and the measured fracture toughness value of CFETR T-L is slightly higher than the one of IGP T-L at room temperature.

As the test temperature increases, the effect of impurities (which can strengthen or weaken the grain boundary cohesion) may become important [61]. Therefore, impurities might be the reason why the fracture behavior of both materials changes. Impurities, segregating to the grain boundaries, can reduce the cohesive strength between sub-grains and/or grains. For IGP, at temperature near $T_{5\%}$, the fracture surface has both intergranular and transgranular brittle fracture patterns since the purity of the material is higher and the grains with $\langle 100 \rangle$ directions parallel to LD (the fraction is around 11%, as shown in Table 5) start to act as a competitive weakest links because of the high Q_{DBT} [46]. As a

result, the fraction of intergranular fracture is reduced to $\sim 10\%$ in IGP T-L near the DBTT. But, for CFETR, the impurity concentration is higher, and therefore, the transgranular brittle fracture is reduced from 60% to 30%.

At temperature exceeding the DBTT, both $\{hkl\}\langle 100 \rangle$ and $\{hkl\}\langle 110 \rangle$ crack system become ductile (the Q_{DBT} is related to the activation energy for the dislocation slip [51]). Thus, ductile fracture features, i.e. dimples and delamination, become evident in the IGP as a result of the plastic deformation and dislocation slip. On the other hand, in the CFETR, some grains still demonstrate cleavage fracture. Therefore, the fracture surface exhibits both dimples and transgranular brittle fracture (around 30% of the fracture area). Keeping in mind that the difference between the texture of IGP T-L and CFETR T-L is not just confined with the texture components that had been mentioned above, the detail of other texture components will require further investigation.

5. Conclusion

The fracture toughness and maximum flexural strain have been assessed for two commercial tungsten grades produced by European and Chinese companies. The grades are produced to comply with ITER specifications and the mechanical tests were performed for the T-L orientation, which is relevant for plasma facing components, accounting for the texture of the materials. On the basis of the obtained results by performing the mechanical tests and microstructural analysis, we come to the following conclusions:

- (i) The fracture toughness and three point bending tests were performed in the temperature range of RT–600 °C, where the transition from ductile to brittle behavior is expected. The temperature dependence of the K_{Jc} and flexural strain follow very similar variation, which suggests that the three point bending tests can be used to explore the temperature bounds of the ductile to brittle transition range with high confidence.
- (ii) The dependence of the fracture surface on temperature (K_{Jc} -T curve) in the transition temperature range can be derived by combination of the three point bending tests and single temperature fracture toughness test. Such approach can be used to assess the DBTT of the neutron irradiated material which is already well pre-characterized in the non-irradiated conditions. If proved to be valid, the approach will enable to reduce the number of samples and tests to construct K_{Jc} -T curve. In this work, we have simulated the construction of the K_{Jc} -T curve for two commercial tungsten

grades, which has been shown to be rather accurate if one overlays the experimental fracture toughness data obtained in the whole transition temperature range. The next step is to demonstrate the robustness of this approach and to perform heat treatments and proton irradiation (generating 1 mm uniform damage) on non-irradiated materials to change its DBTT that should be captured by 3PB tests.

- (iii) Considering that the temperature at which the material deforms up to 5% of flexural strain can be taken as the DBTT (criterion induced in [38]), the fracture toughness at $T_{5\%}$ was calculated for the two grades by interpolating the experimental data and was found to be same for both being equal to 23 MPa \sqrt{m} . The fracture surfaces of the bending samples and disk compact tension samples were compared at $T_{5\%}$ for both materials, and a good correspondence of the microstructural features and morphology observed in the two kinds of samples is found. These findings substantiate further the applicability of the miniaturized three point bending tests to assess the transition temperature range in forged fine-structured tungsten.
- (iv) The transition temperature $T_{5\%}$ of the IGP and CFETR materials is found to be, respectively, $389 \pm 16/-19^\circ\text{C}$ and $305 \pm 12^\circ\text{C}$. The difference in the transition temperature, fracture behavior, and fracture toughness measured for the two materials is discussed on the basis of the microstructure assessed by electron back-scattering diffraction and by fracture surface analysis through scanning electron microscopy.

Acknowledgements

This work has been carried out within the framework of the EUROfusion Consortium and has received funding from the Euratom research and training programme 2014–2018 under grant agreement No 633053. The views and opinions expressed herein do not necessarily reflect those of the European Commission.

References

- [1] T.J. Vogler, J.D. Clayton, Heterogeneous deformation and spall of an extruded tungsten alloy: plate impact experiments and crystal plasticity modeling, *J. Mech. Phys. Solids* 56 (2) (2008) 297–335.
- [2] A.P. Roberts, E.J. Garboczi, Elastic properties of a tungsten-silver composite by reconstruction and computation, *J. Mech. Phys. Solids* 47 (10) (1999) 2029–2055.
- [3] E. Tejado, A.V. Müller, J.H. You, J.Y. Pastor, Evolution of mechanical performance with temperature of W/Cu and W/CuCrZr composites for fusion heat sink applications, *Mater. Sci. Eng. A* 712 (2018) 738–746.
- [4] H. Deng, Z. Xie, Y. Wang, R. Liu, T. Zhang, T. Hao, X. Wang, Q. Fang, C. Liu, Mechanical properties and thermal stability of pure W and W-0.5 wt% ZrC alloy manufactured with the same technology, *Mater. Sci. Eng. A* 715 (2018) 117–125.
- [5] Y. Jiang, L. Zhang, Q. Fang, T. Zhang, X. Wang, T. Hao, C. Liu, Toughness enhancement of tungsten reinforced with short tungsten fibres, *Mater. Sci. Eng. A* 690 (2017) 208–213.
- [6] S.J. Zinkle, J.T. Busby, Structural materials for fission & fusion energy, *Mater. Today* 12 (11) (2009) 12–19.
- [7] S.J. Zinkle, Fusion materials science: overview of challenges and recent progress, *Phys. Plasmas* 12 (5) (2005) 058101.
- [8] S. Matsuda, K. Tobita, Evolution of the ITER program and prospect for the next-step fusion demo reactors: status of the fusion energy R&D as ultimate source of energy, *J. Nucl. Sci. Technol.* 50 (4) (2013) 321–345.
- [9] M. Rieth, D. Armstrong, B. Dafferner, S. Heger, A. Hoffmann, M.-D. Hofmann, U. Jäntschi, Tungsten as a structural divertor material, *Adv. Sci. Technol.* 73 (2010) 11–21.
- [10] A. Giannattasio, Z. Yao, E. Tarleton, S.G. Roberts, Brittle–ductile transitions in polycrystalline tungsten, *Philos. Mag.* 90 (2010) 3947–3959.
- [11] J.M. Steichen, Tensile properties of neutron-irradiated Tzm and tungsten, *J. Nucl. Mater.* 60 (1) (1976) 13–19.
- [12] I.V. Gorynin, V.A. Ignatov, V.V. Rybin, S.A. Fabritsiev, V.A. Kazakov, V.P. Chakin, V.A. Tsykanov, V.R. Barabash, Y.G. Prokofyev, Effects of neutron-irradiation on properties of refractory-metals, *J. Nucl. Mater.* 191 (1992) 421–425.
- [13] I. Alexandrov, I.V. Gorynin, *Metallovedenie* 22 (1979) 35.
- [14] T. Hirai, S. Panayotis, V. Barabash, et al., Use of tungsten material for the ITER divertor, *Nucl. Mater. Energy* 9 (2016) 1–7.
- [15] M.Y. Li, E. Werner, J.H. You, Fracture mechanical analysis of tungsten armor failure of a water-cooled divertor target, *Fusion Eng. Des.* 89 (11) (2014) 2716–2725.
- [16] F. Ferroni, X. Yi, K. Arakawa, S.P. Fitzgerald, P.D. Edmonds, S.G. Roberts, High temperature annealing of ion irradiated tungsten, *Acta Mater.* 90 (2015) 380–393.
- [17] J. Gibson, D. Armstrong, S. Roberts, The micro-mechanical properties of ion irradiated tungsten, *Phys. Scr.* T159 (2014).
- [18] D.E.J. Armstrong, X. Yi, E.A. Marquis, S.G. Roberts, Hardening of self ion implanted tungsten and tungsten 5-wt% rhenium, *J. Nucl. Mater.* 432 (1–3) (2013) 428–436.
- [19] B.J. Kim, R. Kasada, A. Kimura, H. Tanigawa, Evaluation of grain boundary embrittlement of phosphorus added F82H steel by SSTT, *J. Nucl. Mater.* 421 (1–3) (2012) 153–159.
- [20] N. Igata, K. Miyahara, C. Tada, D. Blas, G. Lucas, Phenomenological studies of the effects of miniaturization and irradiation on the mechanical-properties of stainless-steels, *Radiat. Eff. Defect Solids* 101 (1–4) (1987) 131–146.
- [21] D. Rupp, S.M. Weygand, Experimental investigation of the fracture toughness of polycrystalline tungsten in the brittle and semi-brittle regime, *J. Nucl. Mater.* 386–88 (2009) 591–593.
- [22] D. Rupp, S. Weygand, Anisotropic fracture behaviour and brittle-to-ductile transition of polycrystalline tungsten, *Philos. Mag.* 90 (30) (2010) 4055–4069.
- [23] E. Gaganidze, D. Rupp, J. Aktaa, Fracture behaviour of polycrystalline tungsten, *J. Nucl. Mater.* 446 (1–3) (2014) 240–245.
- [24] B. Gludovatz, S. Wurster, A. Hoffmann, R. Pippin, Fracture toughness of polycrystalline tungsten alloys, *Int. J. Refract. Met. Hard Mater.* 28 (6) (2010) 674–678.
- [25] S. Wurster, B. Gludovatz, R. Pippin, High temperature fracture experiments on tungsten-rhenium alloys, *Int. J. Refract. Met. Hard Mater.* 28 (6) (2010) 692–697.
- [26] M. Faleschini, H. Kreuzer, D. Kiener, R. Pippin, Fracture toughness investigations of tungsten alloys and SPD tungsten alloys, *J. Nucl. Mater.* 367 (2007) 800–805.
- [27] F.W. Zok, On weakest link theory and Weibull statistics, *J. Am. Ceram. Soc.* 100 (4) (2017) 1265–1268.
- [28] E1921-16, Standard Test Method for Determination of Reference Temperature, T_0 , for Ferritic Steels in the Transition Range, ASTM international, West Conshohocken, PA, USA, 2016.
- [29] R. Margevicius, J. Riedle, P. Gumbsch, Fracture toughness of polycrystalline tungsten under mode I and mixed mode I/II loading, *Mater. Sci. Eng. A* 270 (2) (1999) 197–209.
- [30] J. Ast, M. Göken, K. Durst, Size-dependent fracture toughness of tungsten, *Acta Mater.* 138 (2017) 198–211.
- [31] C. Lu, R. Danzer, F.D. Fischer, Fracture statistics of brittle materials: weibull or normal distribution, *Phys. Rev. E* 65 (6) (2002) 067102.
- [32] R. Danzer, P. Supancic, J. Pascual, T. Lube, Fracture statistics of ceramics–Weibull statistics and deviations from Weibull statistics, *Eng. Fract. Mech.* 74 (18) (2007) 2919–2932.
- [33] R. Doremus, Fracture statistics: a comparison of the normal, Weibull, and Type I extreme value distributions, *J. Appl. Phys.* 54 (1) (1983) 193–198.
- [34] Z. Bertalan, A. Shekhawat, J.P. Sethna, S. Zapperi, Fracture strength: stress concentration, extreme value statistics, and the fate of the Weibull distribution, *Phys. Rev. Appl.* 2 (3) (2014) 034008.
- [35] Z. Baant, Y. Xi, S. Reid, Statistical size effect in quasi-brittle structures: I. Is Weibull theory applicable? *J. Eng. Mech. ASCE* 117 (1991) 2609–2622.
- [36] D. Wu, Y. Li, J. Zhang, L. Chang, D. Wu, Z. Fang, Y. Shi, Effects of the number of testing specimens and the estimation methods on the Weibull parameters of solid catalysts, *Chem. Eng. Sci.* 56 (24) (2001) 7035–7044.
- [37] C. Seal, A. Sherry, Weibull distribution of brittle failures in the transition region, *Procedia Struct. Integr.* 2 (2016) 1668–1675.
- [38] D.H. Lassila, F. Magness, D. Freeman, Ductile–Brittle Transition Temperature testing of tungsten using the three-point bend test, Lawrence Livermore National Lab., CA (United States), 1991.
- [39] Z.M. Xie, R. Liu, S. Miao, X.D. Yang, T. Zhang, X.P. Wang, Q.F. Fang, C.S. Liu, G.N. Luo, Y.Y. Lian, X. Liu, Extraordinary high ductility/strength of the interface designed bulk W–ZrC alloy plate at relatively low temperature, *Sci. Rep.* 5 (2015) (UK).
- [40] V. Krsjak, S. Wei, S. Antusch, Y. Dai, Mechanical properties of tungsten in the transition temperature range, *J. Nucl. Mater.* 450 (1–3) (2014) 81–87.
- [41] E1820-15a, Standard Test Method for Measurement of Fracture toughness, ASTM International, 2015.
- [42] E290-14, Standard Test Methods for Bend Testing of Material for Ductility, ASTM international, 2014.
- [43] A. Dubinko, D. Terentyev, A. Bakaeva, M. Hernández-Mayoral, G. De Temmerman, L. Buzi, J.-M. Noterdaeme, B. Unterberg, Sub-surface microstructure of single and polycrystalline tungsten after high flux plasma exposure studied by TEM, *Appl. Surf. Sci.* 393 (2017) 330–339.
- [44] E 399-12, Standard Test Method for Linear-Elastic Plane Strain Fracture Toughness KIC of Metallic Materials, ASTM international, 2012.
- [45] J. Ast, J. Schwiedrzik, J. Wehrs, D. Frey, M.N. Polyakov, J. Michler, X. Maeder, The brittle–ductile transition of tungsten single crystals at the micro-scale, *Mater. Des.* 152 (2018) 168–180.
- [46] A. Giannattasio, S.G. Roberts, Strain-rate dependence of the brittle-to-ductile transition temperature in tungsten, *Philos. Mag.* 87 (17) (2007) 2589–2598.
- [47] P. Gumbsch, J. Riedle, A. Hartmaier, H.F. Fischmeister, Controlling factors for the brittle-to-ductile transition in tungsten single crystals, *Science* 282 (5392) (1998) 1293–1295.
- [48] D. Rupp, S.M. Weygand, Loading rate dependence of the fracture toughness of polycrystalline tungsten, *J. Nucl. Mater.* 417 (1–3) (2011) 477–480.
- [49] P. Gumbsch, Brittle fracture and the brittle-to-ductile transition of tungsten, *J. Nucl. Mater.* 323 (2–3) (2003) 304–312.
- [50] W. Tyson, W.J.S.S. Miller, Surface free energies of solid metals: estimation from liquid surface tension measurements, *Surf. Sci.* 62 (1) (1977) 267–276.
- [51] J. Reiser, J. Hoffmann, U. Jäntschi, M. Klimenkov, S. Bonk, C. Bonnekoh, M. Rieth, A. Hoffmann, T. Mrotzek, Ductilisation of tungsten (W): on the shift of the brittle-to-

- ductile transition (BDT) to lower temperatures through cold rolling, *Int. J. Refract. Met. Hard Mater.* 54 (2016) 351–369.
- [52] V. Nikolić, S. Wurster, D. Firneis, R. Pippan, Fracture toughness evaluation of UFG tungsten foil, *Int. J. Refract. Met. Hard Mater.* 76 (2018) 214–225.
- [53] V. Nikolic, S. Wurster, D. Firneis, R. Pippan, Improved fracture behavior and microstructural characterization of thin tungsten foils, *Nucl. Mater. Energy* 9 (2016) 181–188.
- [54] Z.S. Levin, A. Srivastava, D.C. Foley, K.T. Hartwig, Fracture in annealed and severely deformed tungsten, *Mater. Sci. Eng. A* (2018).
- [55] M. Mahler, E. Gaganidze, J. Aktaa, Simulation of anisotropic fracture behaviour of polycrystalline round blank tungsten using cohesive zone model, *J. Nucl. Mater.* 502 (2018) 213–219.
- [56] C. Bonnekoh, A. Hoffmann, J. Reiser, The brittle-to-ductile transition in cold rolled tungsten: on the decrease of the brittle-to-ductile transition by 600 K to -65°C , *Int. J. Refract. Met. Hard Mater.* 71 (2018) 181–189.
- [57] C. Bonnekoh, U. Jäntschi, J. Hoffmann, H. Leiste, A. Hartmaier, D. Weygand, A. Hoffmann, J. Reiser, The brittle-to-ductile transition in cold rolled tungsten plates: impact of crystallographic texture, grain size and dislocation density on the transition temperature, *Int. J. Refract. Met. Hard Mater.* 78 (2019) 146–163.
- [58] C. Bohnert, N. Schmitt, S. Weygand, O. Kraft, R. Schwaiger, Fracture toughness characterization of single-crystalline tungsten using notched micro-cantilever specimens, *Int. J. Plast.* 81 (2016) 1–17.
- [59] B. Gludovatz, S. Wurster, T. Weingärtner, A. Hoffmann, R. Pippan, Influence of impurities on the fracture behaviour of tungsten, *Philos. Mag.* 91 (22) (2011) 3006–3020.
- [60] C. Prakash, H. Lee, M. Alucozai, V. Tomar, An analysis of the influence of grain boundary strength on microstructure dependent fracture in polycrystalline tungsten, *Int. J. Fract.* 199 (1) (2016) 1–20.
- [61] J. Morniroli, M. Gantois, M. Lahaye, Brittle fracture of polycrystalline tungsten, *J. Mater. Sci.* 20 (1) (1985) 199–206.